

Influence of Surface Groups on Electrochemical Properties of Molten Salt Synthesized $\text{Ti}_3\text{C}_2\text{T}_x$ in Mild Aqueous Electrolytes

Bin Guan,^[a] Guoliang Ma,^[a] and Zifeng Lin^{*[a]}

MXene, notable for its excellent electrical conductivity and tunable surface groups, has garnered widespread attention in the field of electrochemical energy storage. Here, $\text{Ti}_3\text{C}_2\text{T}_x$ MXene was synthesized by a Lewis acid molten salt-shielded synthesis (MS³). The surface groups ($-\text{Cl}$, $-\text{O}$) were modified by washing $\text{Ti}_3\text{C}_2\text{T}_x$ samples with various solutions (deionized water, 0.5 M hydrochloric acid (HCl), 0.5 M ammonium persulfate solution (APS)) and/or thermal treatments under an argon atmosphere at 300 °C, 500 °C, and 700 °C. It is shown that deionized water and HCl solution washing have minimal impact on the surface groups, while APS washing can increase the content of $-\text{O}$ surface group. Conversely, thermal treatment may remove the

$-\text{O}$. Electrochemical charge storage behavior of these $\text{Ti}_3\text{C}_2\text{T}_x$ variants were further investigated in a 1 M acetate electrolyte buffered at pH = 5.0. It is indicated that the $-\text{Cl}$ surface group is electrochemically inert, whereas the $-\text{O}$ may significantly improve the charge storage performance. $\text{Ti}_3\text{C}_2\text{T}_x$ with high $-\text{O}$ content delivered an impressive maximum capacity of 155 Cg⁻¹. This research underscores the crucial role of surface groups on the electrochemical performance of $\text{Ti}_3\text{C}_2\text{T}_x$ in mild aqueous electrolytes, offering valuable insights for future modifications and applications of $\text{Ti}_3\text{C}_2\text{T}_x$ in energy storage technologies.

1. Introduction

With growing global concerns about carbon emissions, the utilization of renewable energy has been progressively optimized and enhanced.^[1–3] MXene, a novel two-dimensional transition metal carbide/nitride, is regarded as a potential material for renewable energy conversion and storage.^[4,5] Derived by selectively etching the A-layer atoms from MAX phase materials, its general formula is $\text{M}_{n+1}\text{X}_n\text{T}_x$, where M denotes early transition metals, X signifies carbon or nitrogen, and T_x represents surface groups ($-\text{F}$, $-\text{Cl}$, $-\text{OH}$, $-\text{O}$, etc.).^[6] Studies indicate that the surface groups of MXene can be chemically modified, and variations in T_x can change electrochemical properties of MXene.^[7–10] Typically, MXene is prepared by etching A-layer atoms using hydrofluoric acid, the resultant MXene usually bears $-\text{F}$, $-\text{OH}$, or $-\text{O}$ terminations.^[11] The use of HF and fluorine-containing acidic solutions in these methods poses safety concerns.^[12]

In 2019, Li^[13,14] et al. introduced a safer, environmentally friendly approach to synthesize MXene using Lewis acid salts, such as CuCl_2 and ZnCl_2 , as etching agents, typically yielding surface groups like $-\text{Cl}$, $-\text{Br}$, and $-\text{O}$. Due to the relative instability of $-\text{Cl}$ and $-\text{Br}$, MXene is highly prone to introducing $-\text{O}$ group during an aqueous solution washing process.^[15] It has

been observed that with the introduction of the $-\text{O}$ group, MS-MXene serves as an anode for lithium-ion intercalation, exhibiting enhanced performance in organic electrolytes.^[16] However, MS- $\text{Ti}_3\text{C}_2\text{T}_x$ ($\text{T}_x=\text{Cl}, \text{Br}$) shows worse performance than HF- $\text{Ti}_3\text{C}_2\text{T}_x$ ($\text{T}_x=\text{O}, \text{OH}, \text{F}$) and LiF/HCl- $\text{Ti}_3\text{C}_2\text{T}_x$ ($\text{T}_x=\text{O}, \text{OH}, \text{F}$) in aqueous electrolytes.

In 2022, Kosuke Kawai^[10] et al. concluded that MS- $\text{Ti}_3\text{C}_2\text{T}_x$ ($\text{T}_x=\text{Cl}, \text{O}$) showed worse performance than HF- $\text{Ti}_3\text{C}_2\text{T}_x$ ($\text{T}_x=\text{O}, \text{OH}, \text{F}$) and LiF/HCl- $\text{Ti}_3\text{C}_2\text{T}_x$ ($\text{T}_x=\text{O}, \text{OH}, \text{F}$) in aqueous electrolytes (0.5 M H_2SO_4 , 0.5 M Li_2SO_4 , 0.5 M Na_2SO_4 , etc.). Interestingly, Wang^[17] et al. showed that MS- $\text{Ti}_3\text{C}_2\text{T}_x$ ($\text{T}_x=\text{Cl}, \text{Br}$) exhibited high pseudocapacitance in mild aqueous solutions (1 M AlCl_3 and 1 M acetate buffer). These studies suggest the important role of surface groups on electrochemical properties of MXene in aqueous electrolytes. However, understanding the influence of different surface groups, especially new surface groups introduced by molten salt synthesis route, on electrochemical properties is far from clear.

In this study, $\text{Ti}_3\text{C}_2\text{T}_x$ with $-\text{Cl}$ and $-\text{O}$ surface groups were synthesized by molten salt-shielded synthesis.^[18] Aqueous solutions washing and thermal treatments were applied to tune the surface groups of $\text{Ti}_3\text{C}_2\text{T}_x$. $-\text{O}$ rich $\text{Ti}_3\text{C}_2\text{T}_x$ can be achieved by APS washing, while $\text{Ti}_3\text{C}_2\text{T}_x$ washed by other solutions are characterized with $-\text{Cl}$ rich surface group. $\text{Ti}_3\text{C}_2\text{T}_x$ treated with annealing at different temperatures under an Ar atmosphere led to the removal of $-\text{O}$. In addition, impacts of $-\text{Cl}$ and $-\text{O}$ surface groups on electrochemical properties of $\text{Ti}_3\text{C}_2\text{T}_x$ in acetic acid buffer solution was investigated. Findings suggest that the presence of the $-\text{O}$ surface group improves the electrochemical performance of MS- $\text{Ti}_3\text{C}_2\text{T}_x$, while $-\text{Cl}$ surface group exhibits no electrochemical activity.

[a] B. Guan, G. Ma, Prof. Z. Lin
College of Materials Science and Engineering, Sichuan University, Chengdu, China
E-mail: linzifeng@vip.163.com
linzifeng@scu.edu.cn

 Supporting information for this article is available on the WWW under
<https://doi.org/10.1002/batt.202400153>

Experimental Section

Preparation of $\text{Ti}_3\text{C}_2\text{T}_x$ MXene

To synthesize $\text{Ti}_3\text{C}_2\text{T}_x$ MXene, the previously reported molten salt-shielded method was utilized.^[16] Briefly, Ti_3AlC_2 (400 mesh) was used as a precursor. A eutectic mixture of NaCl and KCl served as the salt bed, shielding the reaction from atmospheric interference. NiCl_2 was employed as the etchant with a molar ratio of Ti_3AlC_2 , NiCl_2 , NaCl, and KCl set to 1:6:10:10. NiCl_2 , NaCl, and KCl were first ground together for ten minutes to ensure thorough mixing. Ti_3AlC_2 was then placed at the bottom of a crucible, and the mixed etchant and salt bed were layered over it. The crucible was subsequently placed in a muffle furnace, heated at a rate of 10°C/min to 750°C, held for 25 minutes to complete etching, and cooled to room temperature. The resultant mixture contained $\text{Ti}_3\text{C}_2\text{T}_x$ MXene, salts, and elemental nickel. This mixture was partitioned into three parts in weight ratios of 1:1:4 and separately immersed in deionized water, 0.5 M HCl, and 0.5 M APS for 0.5 hours at room temperature. Deionized water and a magnet were used to remove solutes and nickel. The retrieved products were dried in a vacuum oven at 60°C for 10 hours. The dried products were designated as $\text{Ti}_3\text{C}_2\text{T}_x\text{--H}_2\text{O}$, $\text{Ti}_3\text{C}_2\text{T}_x\text{--HCl}$, and $\text{Ti}_3\text{C}_2\text{T}_x\text{--APS}$. Finally, $\text{Ti}_3\text{C}_2\text{T}_x\text{--APS}$ was divided into four equal parts, three of which were subjected to heat treatments in an argon-filled tube furnace. Heating rates of 10°C/min were applied to reach 300°C, 500°C, and 700°C, respectively, held for 30 minutes, and cooled to ambient conditions. The products were labeled $\text{Ti}_3\text{C}_2\text{T}_x\text{-300}$, $\text{Ti}_3\text{C}_2\text{T}_x\text{-500}$, and $\text{Ti}_3\text{C}_2\text{T}_x\text{-700}$.

Material Characterization

The crystal structure of $\text{Ti}_3\text{C}_2\text{T}_x$ MXene was analyzed using an X-ray diffractometer (DX-2700) with Cu K α radiation ($\lambda=0.15406$ nm) over a 20 scan range of 5° to 70°. The morphology and elemental distribution of $\text{Ti}_3\text{C}_2\text{T}_x$ MXene were examined using a scanning electron microscope (SEM, JSM-7900F) and an energy dispersive X-ray spectrometer (EDS, Ultima MAX 65). The surface chemical composition and states of $\text{Ti}_3\text{C}_2\text{T}_x$ MXene samples were further probed using X-ray photoelectron spectroscopy (XPS, AXIS Supra) with C 1s set to 284.6 eV as a reference during the XPS analysis. The electrical conductivity of $\text{Ti}_3\text{C}_2\text{T}_x$ MXene was tested using the four-probe resistance measurement (ST-2722), with the pressure range from 2 MPa to 20 MPa.

Electrode Fabrication

$\text{Ti}_3\text{C}_2\text{T}_x\text{--H}_2\text{O}$, $\text{Ti}_3\text{C}_2\text{T}_x\text{--HCl}$, $\text{Ti}_3\text{C}_2\text{T}_x\text{--APS}$, $\text{Ti}_3\text{C}_2\text{T}_x\text{-300}$, $\text{Ti}_3\text{C}_2\text{T}_x\text{-500}$, $\text{Ti}_3\text{C}_2\text{T}_x\text{-700}$, and activated carbon (YP80) (70 mg each) were individually combined with 20 mg acetylene black and 16.67 mg of 60% PTFE solution, and then laminating them to form films. Finally, the films were dried at 60°C for 5 hours in a vacuum oven and cut into electrodes with a diameter of 8 mm and mass load from 0.8 to 1.4 mg.

Electrochemical Characterization

Electrochemical measurements were carried out on a Bio-Logic VSP-300 electrochemical workstation. Swagelok cells were used for testing with various $\text{Ti}_3\text{C}_2\text{T}_x$ electrodes serving as working electrodes, activated carbon (YP80) as the counter electrode, and $\text{Hg}/\text{Hg}_2\text{SO}_4$ as the reference electrode. An electrolyte was prepared by mixing 1 M acetic acid and 1 M sodium acetate in a 5.9:14.1 volume ratio, resulting in a pH=5 buffer solution. This solution was degassed with Ar for 10 minutes prior to testing. Glass fiber (GF/A) was used as the separator, and glassy carbon served as the current

collector. The potential window for testing was between -0.5 to -1.5 V (vs $\text{Hg}/\text{Hg}_2\text{SO}_4$). All cells underwent a preconditioning process at 20 mV s⁻¹ for 20 cycles. Cyclic voltammograms were recorded from 10 to 500 mV s⁻¹. Long-term cycling tests were performed at 50 mV s⁻¹. Galvanostatic charge-discharge tests were conducted at current densities of 2 Ag⁻¹, 5 Ag⁻¹, 10 Ag⁻¹, and 20 Ag⁻¹.

Calculation of the specific capacity of the MXene electrode was derived from the cathodic portions of the CV curves at various scan rates:

$$Q_m = \frac{\int i dt}{m}$$

Where Q_m represents the specific capacity (C g⁻¹), i is the current (A), t is the time (s), and m is the mass (g) of the active material in the electrode, namely, $\text{Ti}_3\text{C}_2\text{T}_x$ MXene.

To analyze the charge storage mechanism, a power-law relationship was employed to determine the value of b , representing the relationship between the current response and scan rate:

$$i_p = av^b$$

In this relation, i_p is the peak current value, v represents the scan rate, and a and b are specific parameters. The value of b can be deduced from the slope of a plot of $\log(i_p)$ against $\log(v)$.

Computational Details

In this study, the Device Studio program was utilized, providing integrated modular functions for modeling, simulation, and subsequent visualization. Calculations were executed using the DSWPAW software, seamlessly incorporated within the Device Studio framework. The simulation methodology was underpinned by density functional theory (DFT). We employed the Perdew-Burke-Ernzerhof (PBE) functional within the generalized gradient approximation (GGA) paradigm for the exchange-correlation functional. To preclude interactions between adjacent layers, a vacuum layer of 15 Å was established. A 3×3 supercell configuration of $\text{Ti}_3\text{C}_2\text{O}_2/\text{Ti}_3\text{C}_2\text{Cl}_2$ monolayers served as the substrate. For geometrical optimization, the Gamma centered k-point mesh was set to 5×5×1, while a denser mesh of 7×7×1 was adopted for electronic structure calculations in the unit cell of $\text{Ti}_3\text{C}_2\text{O}_2$. In our computational scheme, all atoms were allowed full relaxation, adhering to the force and energy convergence thresholds of 0.02 eV Å⁻¹ and 10⁻⁶ eV, respectively. The cutoff energy was meticulously set at 600 eV. During the adsorption and diffusion processes, the DFT-D3 method with Becke-Jonson damping was implemented to accurately represent the long-range van der Waals interactions. Adsorption energies were quantified using the equation:

$$E_{ad} = E_{\text{Na}/\text{H}+\text{Ti}_3\text{C}_2\text{Cl}_2} - E_{\text{Ti}_3\text{C}_2\text{Cl}_2} - E_{\text{Na}/\text{H}}$$

$$E_{ad} = E_{\text{Na}/\text{H}+\text{Ti}_3\text{C}_2\text{O}_2} - E_{\text{Ti}_3\text{C}_2\text{O}_2} - E_{\text{Na}/\text{H}}$$

where $E_{\text{Na}/\text{H}+\text{Ti}_3\text{C}_2\text{Cl}_2}$ and $E_{\text{Na}/\text{H}+\text{Ti}_3\text{C}_2\text{O}_2}$ denote the total energy of the $\text{Ti}_3\text{C}_2\text{Cl}_2/\text{Ti}_3\text{C}_2\text{O}_2$ system combined with adsorbates. Additionally, to elucidate the charge transfer dynamics during the Na/H adsorption, we simulated the charge density differences. This involved calculating the variance in electron charge densities between Na/H and $\text{Ti}_3\text{C}_2\text{Cl}_2/\text{Ti}_3\text{C}_2\text{O}_2$, and the electronic charge density of the entire adsorption system.

2. Results and Discussion

Figure 1a presents the XRD patterns of $\text{Ti}_3\text{C}_2\text{T}_x$ MXene treated in DI water, 0.5 M HCl, 0.5 M APS, and heat treatment at 300 °C, 500 °C, 700 °C. The (002) diffraction peak of $\text{Ti}_3\text{C}_2\text{T}_x$ is observed at 7.94° (Figure S1), corresponding to an interlayer spacing of 1.11 nm. The obtained diffraction patterns align with previously reported results,^[14,15, 19] confirming the successful synthesis of $\text{Ti}_3\text{C}_2\text{T}_x$ MXene. The diffraction patterns of $\text{Ti}_3\text{C}_2\text{T}_x$ -HCl and $\text{Ti}_3\text{C}_2\text{T}_x$ -APS are basically the same as those of $\text{Ti}_3\text{C}_2\text{T}_x$ -H₂O, exhibiting no significant peak position differences among the samples. Nevertheless, a notable reduction in peak intensity is observed in the APS treated sample, indicating a decrease in crystallinity after the APS washing, a finding consistent with earlier research.^[15] The similarity in the XRD patterns of $\text{Ti}_3\text{C}_2\text{T}_x$ -300 and $\text{Ti}_3\text{C}_2\text{T}_x$ -APS indicates that the heat treatment at 300 °C did not induce noticeable phase changes in the material. The diffraction pattern of $\text{Ti}_3\text{C}_2\text{T}_x$ -500 reveals the emergence of anatase titanium dioxide peaks in addition to the inherent $\text{Ti}_3\text{C}_2\text{T}_x$ peaks, indicating the in-situ oxidation of the -O surface group into anatase titanium dioxide post the 500 °C heat treatment.^[20] At 700 °C, peaks corresponding to both anatase and rutile phases of TiO_2 are observed,^[20] and the characteristic peaks of $\text{Ti}_3\text{C}_2\text{T}_x$ are completely absent. This suggests that $\text{Ti}_3\text{C}_2\text{T}_x$ has been severely oxidized at this temperature, leading to the destruction of its structure. Figures 1b-f correspond to the SEM images of $\text{Ti}_3\text{C}_2\text{T}_x$ -H₂O, $\text{Ti}_3\text{C}_2\text{T}_x$ -HCl, $\text{Ti}_3\text{C}_2\text{T}_x$ -APS, $\text{Ti}_3\text{C}_2\text{T}_x$ -300, and $\text{Ti}_3\text{C}_2\text{T}_x$ -500, where the typical accordion-like layered structure can be observed. Figure 1g shows the SEM image of $\text{Ti}_3\text{C}_2\text{T}_x$ -700, where a significant alteration in the layered structure is evident, correlating with the disappearance of the characteristic peaks of $\text{Ti}_3\text{C}_2\text{T}_x$ in the XRD analysis.

The results obtained from the Energy Dispersive Spectroscopy (EDS) analysis (Figure S2-6) reveal a uniform distribution of the elements titanium (Ti), carbon (C), oxygen (O), and chlorine (Cl) within the sample. The concentrations of aluminum

(Al) and nickel (Ni) are negligible (Table S1), indicating successful etching of the sample and the effective removal of Ni through magnetic separation.^[15] Additionally, the total absence of chlorine (Cl) in the 700 °C treated sample (Figure S7 and Table S1) indicates that the product has been severely oxidized.

The surface state of $\text{Ti}_3\text{C}_2\text{T}_x$ is further investigated by X-ray photoelectron spectroscopy (XPS) analysis. Figure S8 presents the full spectrum and the high-resolution C 1s spectrum used for charge calibration of the samples. In the full spectrum, the signals of Ti 2p, O 1s, and C 1s are clearly visible at ~459, ~532, and ~285 eV, respectively.^[14] The O 1s signal, markedly pronounced in $\text{Ti}_3\text{C}_2\text{T}_x$ -APS, may indicate a predominance of -O surface group in comparison to the other variants. In the high-resolution C 1s spectrum, the C-Ti-T_x signal disappears after the sample is heat-treated at 700 °C, indicating the damage of the $\text{Ti}_3\text{C}_2\text{T}_x$ structure. Figures 2a-c display the high-resolution spectra of Ti 2p, O 1s, and Cl 2p of the samples. The deconvolution of Ti 2p spectrum (Figure 2a) reveals peaks at 454.8(460.8), 456.0(461.8), 458.3(464.1), and 458.9(464.9) eV, corresponding to Ti-C(I), Ti-C(II), Ti-Cl, and Ti-O bonds, respectively.^[14,21, 22] After APS washing, the intensity of the Ti-O bond significantly increases, possibly due to an increase in -O surface group or partial surface oxidation.^[14] After heat treatment at 700 °C, the Ti-C(I), Ti-C(II), and Ti-Cl bonds disappear completely, suggesting the destruction of the $\text{Ti}_3\text{C}_2\text{T}_x$ structure, and the Ti-O bond shifts to 459.2 eV, likely due to excessive oxidation at 700 °C leading to a higher oxidation state of Ti.^[23] In the O 1s spectrum (Figure 2b), peaks at 530.2, 531.2, 532.1, and 533.6 eV correspond to Ti-O, C-Ti-O_x, Al-O, and H₂O, respectively.^[13,16, 22] The C-Ti-O_x could attribute to the -O surface group of $\text{Ti}_3\text{C}_2\text{T}_x$, and Ti-O is due to the formation of TiO_2 through partial surface oxidation.^[14] After APS washing, the peak intensity of C-Ti-O_x significantly increases. With increasing heat treatment temperature, the peak intensity of C-Ti-O_x gradually decreases, while the peak intensity of Ti-O increases, especially after heat treatment at 500 °C and 700 °C. These

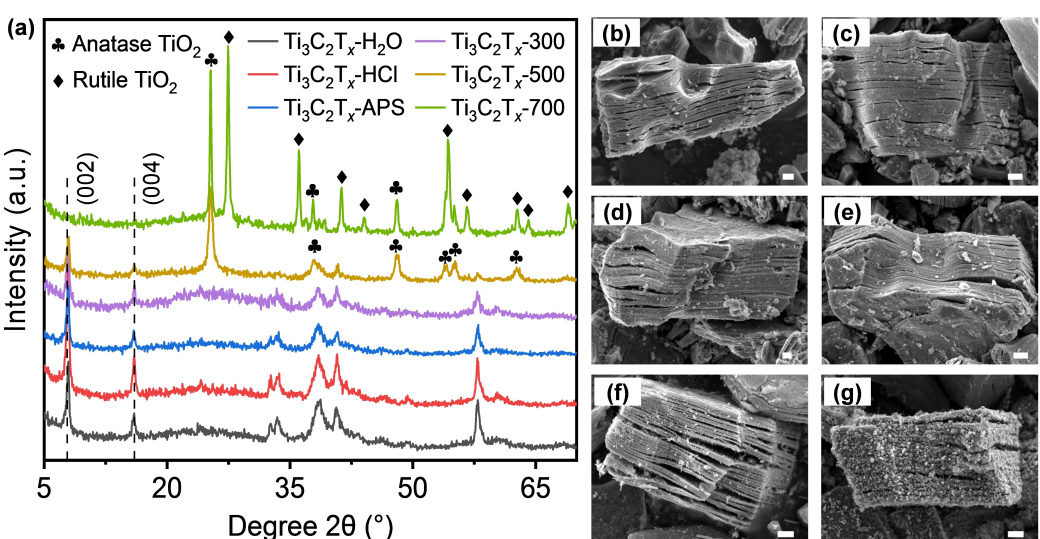


Figure 1. (a) XRD patterns of $\text{Ti}_3\text{C}_2\text{T}_x$ -H₂O, $\text{Ti}_3\text{C}_2\text{T}_x$ -HCl, $\text{Ti}_3\text{C}_2\text{T}_x$ -APS, $\text{Ti}_3\text{C}_2\text{T}_x$ -300, $\text{Ti}_3\text{C}_2\text{T}_x$ -500, and $\text{Ti}_3\text{C}_2\text{T}_x$ -700. SEM images of (b) $\text{Ti}_3\text{C}_2\text{T}_x$ -H₂O, (c) $\text{Ti}_3\text{C}_2\text{T}_x$ -HCl, (d) $\text{Ti}_3\text{C}_2\text{T}_x$ -APS, (e) $\text{Ti}_3\text{C}_2\text{T}_x$ -300, (f) $\text{Ti}_3\text{C}_2\text{T}_x$ -500, and (g) $\text{Ti}_3\text{C}_2\text{T}_x$ -700. The scale bar is 1 μm.

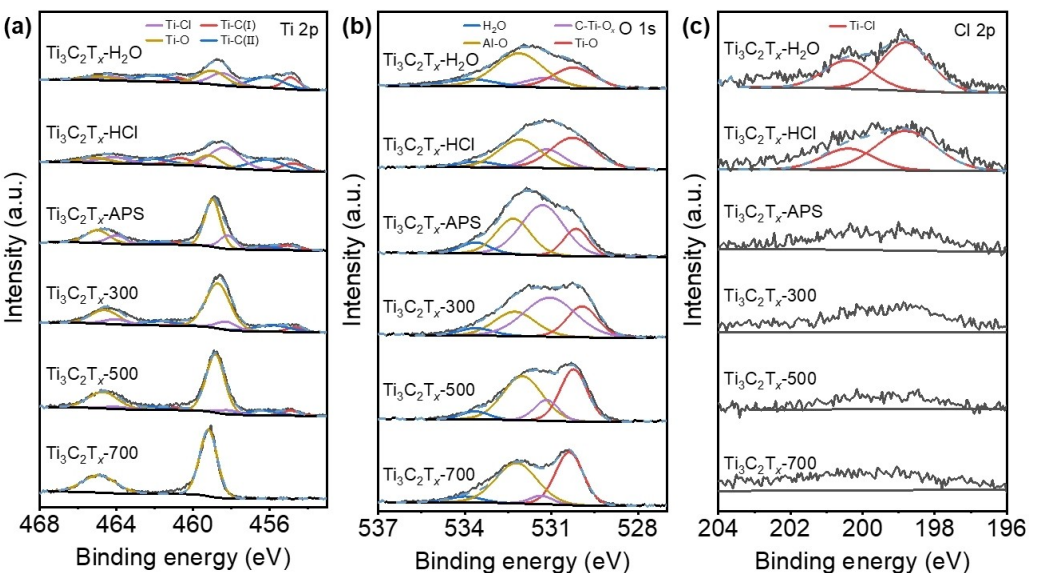


Figure 2. High-resolution XPS spectra for (a) Ti 2p, (b) O 1s, and (c) Cl 2p of $\text{Ti}_3\text{C}_2\text{T}_x\text{-H}_2\text{O}$, $\text{Ti}_3\text{C}_2\text{T}_x\text{-HCl}$, $\text{Ti}_3\text{C}_2\text{T}_x\text{-APS}$, $\text{Ti}_3\text{C}_2\text{T}_x\text{-300}$, $\text{Ti}_3\text{C}_2\text{T}_x\text{-500}$, and $\text{Ti}_3\text{C}_2\text{T}_x\text{-700}$.

results suggest that APS washing endows the surface of $\text{Ti}_3\text{C}_2\text{T}_x$ with abundant $-\text{O}$ surface group, but heat treatment above 300°C may significantly remove the surface groups, and leading to the formation of TiO_2 . Figure 2c shows distinct Cl 2p signals for $\text{Ti}_3\text{C}_2\text{T}_x\text{-H}_2\text{O}$ and $\text{Ti}_3\text{C}_2\text{T}_x\text{-HCl}$, which are attributable to the $-\text{Cl}$ surface group.^[13] After APS washing, the Cl 2p signal weakens significantly, and in conjunction with the previous analysis of $-\text{O}$ surface group content, it is believed that APS washing replaces a large number of $-\text{Cl}$ surface group with $-\text{O}$. Overall, $\text{Ti}_3\text{C}_2\text{T}_x\text{-APS}$ exhibited the highest abundance of $-\text{O}$ surface group, followed by $\text{Ti}_3\text{C}_2\text{T}_x\text{-300}$ and $\text{Ti}_3\text{C}_2\text{T}_x\text{-500}$. In contrast, $\text{Ti}_3\text{C}_2\text{T}_x\text{-H}_2\text{O}$ and $\text{Ti}_3\text{C}_2\text{T}_x\text{-HCl}$ showed a higher concentration of $-\text{Cl}$ group, but a lower presence of $-\text{O}$ group. The primary constituents of $\text{Ti}_3\text{C}_2\text{T}_x\text{-700}$ were identified as anatase and rutile phases of TiO_2 .

A four-probe method was employed to measure the electrical conductivity of $\text{Ti}_3\text{C}_2\text{T}_x\text{-H}_2\text{O}$ and $\text{Ti}_3\text{C}_2\text{T}_x\text{-APS}$ powders, as illustrated in Figure S9. At a pressure of 20 MPa, the conductivity of $\text{Ti}_3\text{C}_2\text{T}_x\text{-H}_2\text{O}$ was 15.5 Scm^{-1} , while that of $\text{Ti}_3\text{C}_2\text{T}_x\text{-APS}$ was 0.157 Scm^{-1} . This indicates that the electrical conductivity of $-\text{O}$ surface group is lower than that of $-\text{Cl}$, which is consistent with previous reports.^[24] To investigate the impact of varying $-\text{Cl}$ and $-\text{O}$ surface groups contents on the electrochemical properties of samples, electrodes fabricated from $\text{Ti}_3\text{C}_2\text{T}_x\text{-H}_2\text{O}$, $\text{Ti}_3\text{C}_2\text{T}_x\text{-HCl}$, $\text{Ti}_3\text{C}_2\text{T}_x\text{-APS}$, $\text{Ti}_3\text{C}_2\text{T}_x\text{-300}$, $\text{Ti}_3\text{C}_2\text{T}_x\text{-500}$, and $\text{Ti}_3\text{C}_2\text{T}_x\text{-700}$ were employed as working electrodes. YP80 activated carbon served as the counter electrode, $\text{Hg}/\text{Hg}_2\text{SO}_4$ as the reference electrode, and a $\text{pH}=5$ acetic acid buffer solution was used as the electrolyte in a three-electrode Swagelok cell for testing. Figure 3a present the linear sweep voltammetry (LSV) curves of $\text{Ti}_3\text{C}_2\text{T}_x\text{-H}_2\text{O}$, $\text{Ti}_3\text{C}_2\text{T}_x\text{-HCl}$, $\text{Ti}_3\text{C}_2\text{T}_x\text{-APS}$, $\text{Ti}_3\text{C}_2\text{T}_x\text{-300}$, $\text{Ti}_3\text{C}_2\text{T}_x\text{-500}$, and $\text{Ti}_3\text{C}_2\text{T}_x\text{-700}$ at a scan rate of 20 mVs^{-1} . A comparison of the curves reveals that $\text{Ti}_3\text{C}_2\text{T}_x\text{-APS}$, $\text{Ti}_3\text{C}_2\text{T}_x\text{-300}$, and $\text{Ti}_3\text{C}_2\text{T}_x\text{-500}$ exhibit redox peaks between -1 and -1.5 V , whereas $\text{Ti}_3\text{C}_2\text{T}_x\text{-H}_2\text{O}$, $\text{Ti}_3\text{C}_2\text{T}_x\text{-HCl}$, and

$\text{Ti}_3\text{C}_2\text{T}_x\text{-700}$ show direct hydrogen evolution reaction (HER) at -1.2 V and no cathodic current peaks were observed. The different on-set potentials of HER can be explained by the variation of surface groups on MXene.

To confirm the different redox activity of these electrodes, CVs with the same fix operation potential range from -0.5 to -1.5 V versus $\text{Hg}/\text{Hg}_2\text{SO}_4$ were measured (Figure 3b). It is clearly shown that $\text{Ti}_3\text{C}_2\text{T}_x\text{-H}_2\text{O}$, $\text{Ti}_3\text{C}_2\text{T}_x\text{-HCl}$, and $\text{Ti}_3\text{C}_2\text{T}_x\text{-700}$ samples do not present any reversible redox peaks as can be observed in $\text{Ti}_3\text{C}_2\text{T}_x\text{-APS}$, $\text{Ti}_3\text{C}_2\text{T}_x\text{-300}$, and $\text{Ti}_3\text{C}_2\text{T}_x\text{-500}$. $\text{Ti}_3\text{C}_2\text{T}_x\text{-APS}$ exhibits the largest redox peaks and the highest capacity (132 Cg^{-1}), followed by $\text{Ti}_3\text{C}_2\text{T}_x\text{-300}$ and $\text{Ti}_3\text{C}_2\text{T}_x\text{-500}$ with gradually weakening redox peaks and capacities of 104 Cg^{-1} and 57 Cg^{-1} , respectively. $\text{Ti}_3\text{C}_2\text{T}_x\text{-H}_2\text{O}$, $\text{Ti}_3\text{C}_2\text{T}_x\text{-HCl}$, and $\text{Ti}_3\text{C}_2\text{T}_x\text{-700}$ show very low capacities. These results correspond well with the changes in the content of $-\text{O}$ surface group in the samples, where $\text{Ti}_3\text{C}_2\text{T}_x\text{-APS}$, with the highest amount of $-\text{O}$ surface group, exhibits the best electrochemical performance, followed by $\text{Ti}_3\text{C}_2\text{T}_x\text{-300}$ and $\text{Ti}_3\text{C}_2\text{T}_x\text{-500}$. Samples with a negligible presence of $-\text{O}$ surface group, such as $\text{Ti}_3\text{C}_2\text{T}_x\text{-H}_2\text{O}$ and $\text{Ti}_3\text{C}_2\text{T}_x\text{-HCl}$, show poor electrochemical performance. In other words, the content of $-\text{O}$ surface group is a key factor in determining whether $\text{Ti}_3\text{C}_2\text{T}_x$ exhibits high charge storage performance. The primary components of $\text{Ti}_3\text{C}_2\text{T}_x\text{-700}$ are anatase and rutile TiO_2 , thus it could be inferred that anatase and rutile TiO_2 have almost no electrochemical activity in this system, ruling out the possibility that the redox peaks in $\text{Ti}_3\text{C}_2\text{T}_x\text{-500}$ are due to anatase TiO_2 . Figure S10 and Figure 3c respectively show the CV curves of the samples at different scan rates (10 mVs^{-1} to 500 mVs^{-1}) and the corresponding capacity-scan rate plots. It is observed that $\text{Ti}_3\text{C}_2\text{T}_x\text{-APS}$ maintains the highest capacity at various scan rates. Figure 3d presents the b-values calculated from the peak currents at different scan rates of the samples, with $\text{Ti}_3\text{C}_2\text{T}_x\text{-APS}$, $\text{Ti}_3\text{C}_2\text{T}_x\text{-300}$, and $\text{Ti}_3\text{C}_2\text{T}_x\text{-500}$ having b-values of 0.67 , 0.67 , and 0.76 ,

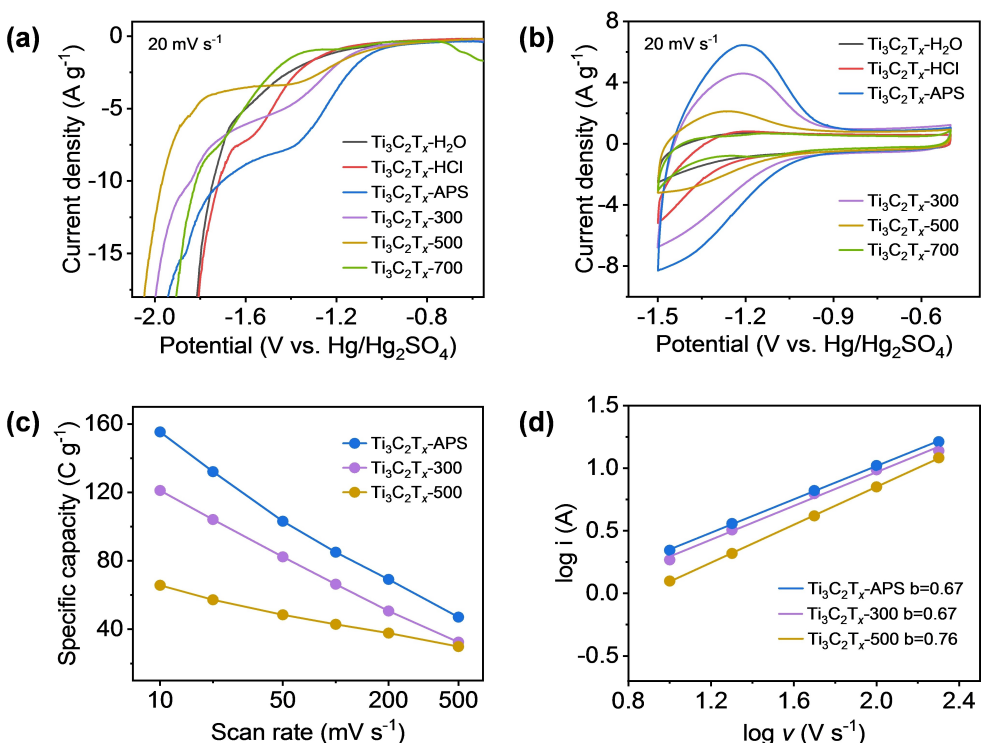


Figure 3. (a) LSV profiles at 20 mV s^{-1} and (b) CV profiles at 20 mV s^{-1} in 1 M acetate (buffered at $\text{pH}=5.0$). (c) Specific capacities at various scan rates and (d) b-values calculated from the CV profiles of $\text{Ti}_3\text{C}_2\text{T}_x\text{-APS}$, $\text{Ti}_3\text{C}_2\text{T}_x\text{-300}$, and $\text{Ti}_3\text{C}_2\text{T}_x\text{-500}$.

respectively, which fall between 0.5 and 0.8, indicating that the electrochemical process involves both diffusion-controlled and surface-controlled process.^[25] Figure S12 shows the CV changes of $\text{Ti}_3\text{C}_2\text{T}_x\text{-H}_2\text{O}$, $\text{Ti}_3\text{C}_2\text{T}_x\text{-HCl}$, $\text{Ti}_3\text{C}_2\text{T}_x\text{-APS}$, $\text{Ti}_3\text{C}_2\text{T}_x\text{-300}$, $\text{Ti}_3\text{C}_2\text{T}_x\text{-500}$, and $\text{Ti}_3\text{C}_2\text{T}_x\text{-700}$ during a long cycling process, where the CV shapes remain stable throughout the cycles, except for $\text{Ti}_3\text{C}_2\text{T}_x\text{-500}$, which shows enhanced redox peaks. The enhancement of the redox peaks in $\text{Ti}_3\text{C}_2\text{T}_x\text{-500}$ may be attributed to an increase in the content of $-\text{O}$ group during the cycling process as $-\text{Cl}$ group are detached during thermal treatment. Figure S13 presents the capacity and coulombic efficiency of samples during long cycling. After 20 cycles, the capacities of $\text{Ti}_3\text{C}_2\text{T}_x\text{-H}_2\text{O}$, $\text{Ti}_3\text{C}_2\text{T}_x\text{-HCl}$, $\text{Ti}_3\text{C}_2\text{T}_x\text{-APS}$, $\text{Ti}_3\text{C}_2\text{T}_x\text{-300}$, $\text{Ti}_3\text{C}_2\text{T}_x\text{-500}$, and $\text{Ti}_3\text{C}_2\text{T}_x\text{-700}$ were 21, 22, 105, 87, 50, and 22 C g^{-1} , respectively, with corresponding Coulombic efficiencies of 85%, 84%, 97%, 96%, 97%, and 83%. $\text{Ti}_3\text{C}_2\text{T}_x\text{-H}_2\text{O}$, $\text{Ti}_3\text{C}_2\text{T}_x\text{-HCl}$, and $\text{Ti}_3\text{C}_2\text{T}_x\text{-700}$ exhibited lower Coulombic efficiencies due to excessive hydrogen evolution caused by a lower hydrogen evolution overpotential, which led to battery failure around 300 cycles. In contrast, $\text{Ti}_3\text{C}_2\text{T}_x\text{-300}$ and $\text{Ti}_3\text{C}_2\text{T}_x\text{-500}$ maintained high Coulombic efficiencies, enabling them to cycle nearly 1000 times. $\text{Ti}_3\text{C}_2\text{T}_x\text{-APS}$ demonstrated outstanding performance over 5000 cycles, maintaining a Coulombic efficiency of 94% after 5000 cycles and a capacity retention rate exceeding 100%. These results indicate that the MXene material rich in $-\text{O}$ group exhibits excellent reversibility and cycle stability.

To elucidate the variations in electrochemical performance among different samples, we performed Density Functional

Theory (DFT) calculations. These calculations aimed to assess the adsorption energies of two cations, H^+ and Na^+ , within the electrolyte used in this study, focusing on $\text{Ti}_3\text{C}_2\text{Cl}_2$ and $\text{Ti}_3\text{C}_2\text{O}_2$. We have detailed the adsorption energy data for H^+ and Na^+ across various sites on these materials in Tables S8 and S9. Table 1 highlights the maximum adsorption energies at all relevant sites for $\text{Ti}_3\text{C}_2\text{Cl}_2$ and $\text{Ti}_3\text{C}_2\text{O}_2$. Notably, $\text{Ti}_3\text{C}_2\text{O}_2$ shows the greater adsorption energies for both cations, suggesting a stronger interaction with H^+/Na^+ . On the other hand, the lower adsorption energy of $\text{Ti}_3\text{C}_2\text{Cl}_2$ for H^+/Na^+ ions suggests a relatively weak interaction between them. Consequently, the $-\text{Cl}$ surface group exhibits almost no energy storage ability. These theoretical findings align well with our electrochemical test results. Figure 4a-c show the differential charge density maps for the adsorption of Na on $\text{Ti}_3\text{C}_2\text{Cl}_2$, Na on $\text{Ti}_3\text{C}_2\text{O}_2$, and H on $\text{Ti}_3\text{C}_2\text{O}_2$, corresponding to the three scenarios with negative adsorption energies listed in Table 1. In these cases, the adsorption site for Na on $\text{Ti}_3\text{C}_2\text{Cl}_2$ is above the Ti atom, for Na on $\text{Ti}_3\text{C}_2\text{O}_2$ it is above the C atom, and for H it is above the O atom. The blue and yellow regions represent the decrease and

Table 1. Adsorption Energies (E_{ad}) of $\text{Ti}_3\text{C}_2\text{Cl}_2$ and $\text{Ti}_3\text{C}_2\text{O}_2$.

Samples	E_{ad} (eV per H^+)	E_{ad} (eV per Na^+)
$\text{Ti}_3\text{C}_2\text{Cl}_2$	1.53	-0.12
$\text{Ti}_3\text{C}_2\text{O}_2$	-0.53	-2.19

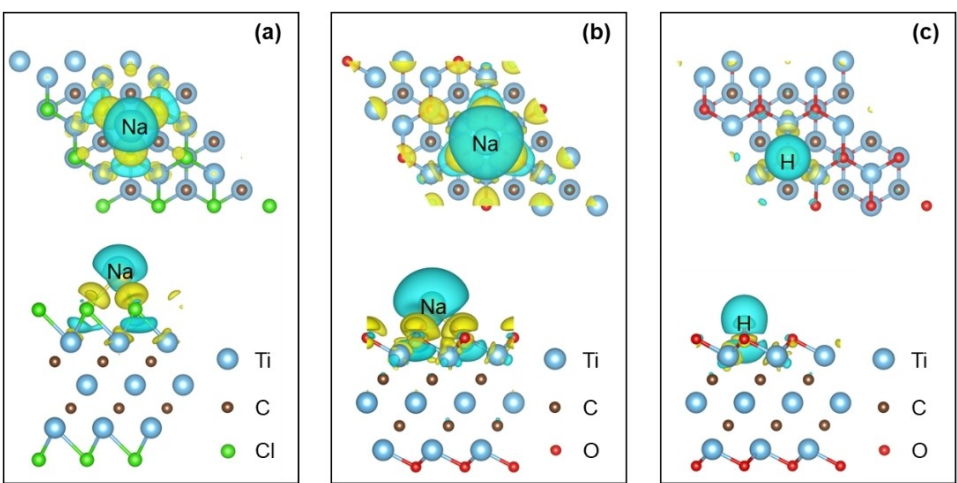


Figure 4. Charge density differences for the Na adsorption on the (a) Ti1 site of $\text{Ti}_3\text{C}_2\text{Cl}_2$ and (b) C1 site of $\text{Ti}_3\text{C}_2\text{O}_2$, (c) for the H adsorption on the O1 site of $\text{Ti}_3\text{C}_2\text{O}_2$.

increase of charge, respectively. Following adsorption, the charge is transferred from one Na/H atom to $\text{Ti}_3\text{C}_2\text{Cl}_2/\text{Ti}_3\text{C}_2\text{O}_2$.

3. Conclusions

In summary, we innovatively synthesized $\text{Ti}_3\text{C}_2\text{T}_x$ using a Lewis acid molten salt-shielded technique, subsequently modifying its surface groups ($-\text{O}$, $-\text{Cl}$) and the proportion of $-\text{O}$ group through various solutions washing and thermal treatments. The electrochemical behaviors of these materials were assessed in mild aqueous electrolytes. Notably, in 1 M acetate buffer electrolyte ($\text{pH}=5$), the $-\text{Cl}$ surface group does not exhibit electrochemical activity, while $\text{Ti}_3\text{C}_2\text{T}_x$ with rich $-\text{O}$ surface group demonstrates superior charge storage performance. Furthermore, as the content of $-\text{O}$ surface group increase, there is an enhanced contribution of diffusion-limited capacity, and the redox peaks become more pronounced. To better elucidate the performance differences among various samples, we employed Density Functional Theory (DFT) calculations to assess the adsorption energies of H^+ and Na^+ in the electrolyte on $\text{Ti}_3\text{C}_2\text{Cl}_2$ and $\text{Ti}_3\text{C}_2\text{O}_2$. The results indicate that the $-\text{O}$ surface group manifests the highest adsorption energies for H^+ and Na^+ , enabling the adsorption of a greater number of cations. These theoretical outcomes align with the results of our electrochemical performance tests, providing a coherent explanation for the charge storage behavior of MS- $\text{Ti}_3\text{C}_2\text{T}_x$ in mild aqueous electrolytes. This work highlights the pivotal role that surface groups play in dictating the electrochemical performance of MS- $\text{Ti}_3\text{C}_2\text{T}_x$. The findings hold significant relevance for the investigation of the electrochemical behavior of MS- $\text{Ti}_3\text{C}_2\text{T}_x$ in aqueous electrolytes, offering valuable insights for future research.

Conflict of Interests

The authors declare no conflict of interest.

Data Availability Statement

The data that support the findings of this study are available from the corresponding author upon reasonable request.

Keywords: MXene · surface groups · molten salt-shielded synthesis · electrochemical charge storage · mild aqueous electrolytes

- [1] F. Jamil, H. M. Ali, M. M. Janjua, *J. Energy Storage* **2021**, *35*, 102322.
- [2] A. Liu, X. Liang, X. Ren, W. Guan, T. Ma, *Electrochim. Energy Rev.* **2021**, *5* (1), 112–144.
- [3] A. Bhat, S. Anwer, K. S. Bhat, M. I. H. Mohideen, K. Liao, A. Qurashi, *NPJ 2D Mater. Appl.* **2021**, *5* (1), 61.
- [4] H. T. A. Awan, L. Kumar, W. P. Wong, R. Walvekar, M. Khalid, *Energies* **2023**, *16* (4), 1977.
- [5] S. Zhao, R. Nivetha, Y. Qiu, X. Guo, *Chin. Chem. Lett.* **2020**, *31* (4), 947–952.
- [6] Z. Lin, H. Shao, K. Xu, P.-L. Taberna, P. Simon, *Trends Chem.* **2020**, *2* (7), 654–664.
- [7] Y. Wu, J. Fu, N. He, J. Liu, T. Hua, C. Qin, H. Hu, *Nano Res.* **2023**, *16* (5), 6780–6788.
- [8] L. Liu, H. Zschiesche, M. Antonietti, B. Daffos, N. V. Tarakina, M. Gibilaro, P. Chamelot, L. Massot, B. Dupoyer, P. L. Taberna, P. Simon, *Adv. Energy Mater.* **2022**, *13* (2), 2202709.
- [9] M. Shen, W. Jiang, K. Liang, S. Zhao, R. Tang, L. Zhang, J. Q. Wang, *Angew. Chem. Int. Ed. Engl.* **2021**, *60* (52), 27013–27018.
- [10] K. Kawai, M. Fujita, R. Iizuka, A. Yamada, M. Okubo, *2D Mater.* **2022**, *10* (1), 014012.
- [11] N. Michael, M. Olha, C. Joshua, P. Volker, L. Jun, H. Lars, G. Yury, W. B. Michel, *ACS Nano* **2012**, *6* (2), 1322–1331.
- [12] C. E. Shuck, K. Ventura-Martinez, A. Goad, S. Uzun, M. Shekhirev, *ACS Chem. Health Saf.* **2021**, *28* (5), 326–338.
- [13] M. Li, J. Lu, K. Luo, Y. Li, K. Chang, K. Chen, J. Zhou, J. Rosen, L. Hultman, P. Eklund, P. O. A. Persson, S. Du, Z. Chai, Z. Huang, Q. Huang, *J. Am. Chem. Soc.* **2019**, *141* (11), 4730–4737.
- [14] Y. Li, H. Shao, Z. Lin, J. Lu, L. Liu, B. Dupoyer, P. O. A. Persson, P. Eklund, L. Hultman, M. Li, K. Chen, X. H. Zha, S. Du, P. Rozier, Z. Chai, E.

- Raymundo-Pinero, P. L. Taberna, P. Simon, Q. Huang, *Nat. Mater.* **2020**, 19 (8), 894–899.
- [15] P. Liu, B. Guan, M. Lu, H. Wang, Z. Lin, *Electrochem. Commun.* **2022**, 136, 107236.
- [16] J. Chen, Q. Jin, Y. Li, H. Shao, P. Liu, Y. Liu, P. L. Taberna, Q. Huang, Z. Lin, P. Simon, *Energy Environ.* **2022**, 6 (2), e12328.
- [17] B. Wang, Q. Fan, L. Xu, J. Liu, C. Dai, M. Tang, K. Liang, P.-L. Taberna, Y. Liu, P. Simon, Z. Lin, *ACS Appl. Energ. Mater.* **2023**, <https://doi.org/10.1021/acsaem.3c02376>.
- [18] P. Liu, P. Xiao, M. Lu, H. Wang, N. Jin, Z. Lin, *Chin. Chem. Lett.* **2023**, 34 (4), 107426.
- [19] M. Li, X. Li, G. Qin, K. Luo, J. Lu, Y. Li, G. Liang, Z. Huang, J. Zhou, L. Hultman, P. Eklund, P. O. A. Persson, S. Du, Z. Chai, C. Zhi, Q. Huang, *ACS Nano* **2021**, 15 (1), 1077–1085.
- [20] F. Kong, X. He, Q. Liu, X. Qi, Y. Zheng, R. Wang, Y. Bai, *Electrochim. Acta* **2018**, 265, 140–150.
- [21] M. Han, X. Yin, H. Wu, Z. Hou, C. Song, X. Li, L. Zhang, L. Cheng, *ACS Appl. Mater. Interfaces* **2016**, 8 (32), 21011–9.
- [22] J. Halim, K. M. Cook, M. Naguib, P. Eklund, Y. Gogotsi, J. Rosen, M. W. Barsoum, *Appl. Surf. Sci.* **2016**, 362, 406–417.
- [23] V. Natu, M. Benchakar, C. Canaff, A. Habrioux, S. Célérier, M. W. Barsoum, *Matter* **2021**, 4 (4), 1224–1251.
- [24] L. Liu, E. Raymundo-Pinero, S. Sunny, P. L. Taberna, P. Simon, *Angew. Chem. Int. Ed. Engl.* **2024**, 63 (14), e202319238.
- [25] C. Choi, D. S. Ashby, D. M. Butts, R. H. DeBlock, Q. Wei, J. Lau, B. Dunn, *Nat. Rev. Mater.* **2019**, 5 (1), 5–19.

Manuscript received: March 5, 2024
Revised manuscript received: April 16, 2024
Accepted manuscript online: May 1, 2024
Version of record online: June 14, 2024